Enhancement of electrical conduction and phonon scattering in $Ga_2O_3(ZnO)_9$ by designing interfaces at the nanoscale

Diana T. Alvarez -Ruiz[1], Feridoon Azough[1],

David Hernandez-Maldonado[2], Demie M. Kepaptsoglou[2], Quentin M. Ramasse[2],

Peter Svec[4], Peter Svec Sr.[4], Robert Freer[1,*]

[1] School of Materials, University of Manchester, Manchester, M13 9PL, U.K.

[2] SuperSTEM Laboratory, STFC Daresbury Campus, Daresbury WA4 4AD, U.K.

[3] Institute of Physics, Slovak Academy of Sciences, Bratislava 845 11, Slovak Republic

*corresponding author: Robert.Freer@manchester.ac.uk

Tel: +44(0)-161-306-3564

ABSTRACT

The $Ga_2O_3(ZnO)_9$ and $In_2O_3(ZnO)_9$ homologous phases have attracted attention as thermoelectrics (TE) due to their layered structures. $Ga_2O_3(ZnO)_9$ exhibits low thermal conductivity, while $In_2O_3(ZnO)_9$ possesses higher electrical conductivity. The thermoelectric properties of the solid solution of $Ga_2O_3(ZnO)_9$ - $In_2O_3(ZnO)_9$ were explored and correlated with changes in the crystal structure. High quality (1-x)$Ga_2O_3(ZnO)_9$ - x$In_2O_3(ZnO)_9$ (x=0.0 to 1.0) ceramics were prepared by the solid-state route using B_2O_3 and Nd_2O_3 as additives. The crystal structures were analysed by XRD, HRTEM and atomic resolution STEM-HAADF-EDS. A layered superstructure with compositional modulations was observed in all samples in the (1-x)$Ga_2O_3(ZnO)_9$ - x$In_2O_3(ZnO)_9$ system. All the ceramics exhibited nanoscale structural features identified as Ga- and In-rich inversion boundaries (IB's). Substitution of 20 mole% In (x=0.2) in the $Ga_2O_3(ZnO)_9$ compounds generated basal and pyramidal indium IB's typically found in the $In_2O_3(ZnO)_m$ system. The $(Ga_{0.8}In_{0.2})_2O_3(ZnO)_9$ compound does not exhibit the structural features of the $Cmcm$ $Ga_2O_3(ZnO)_9$ compound, which is formed by a

stacking of Ga-rich IB's along the pyramidal plane of the wurtzite ZnO, but features that resemble the crystal structure exhibited by the $R\bar{3}m$ $In_2O_3(ZnO)_m$ with basal and pyramidal indium IB's. The structural changes led to improved thermoelectric performance. For example $(Ga_{0.8}In_{0.2})_2O_3(ZnO)_9$ showed low thermal conductivity of 2 W/m·K and high power factor of 150 μW/m·K^2 giving a *ZT* of 0.07 at 900 K. This is the highest *ZT* for $Ga_2O_3(ZnO)_9$ based homologous compounds and is comparable with the highest *ZT* reported for $In_2O_3(ZnO)_9$ homologous compounds.

Key words: ZnO, thermoelectric, homologous compounds, interfaces, inversion boundaries, twin boundaries.

INTRODUCTION

To minimise the environmental impact of power generation from fossil fuels alternative sources are being investigated. Thermoelectrics have many attractions because they can be used to generate electrical power from waste heat without releasing CO_2. For many years Pb- and Te-based alloys have been extensively investigated [1] for thermoelectric applications as they exhibit low thermal conductivity (κ) and relatively high electrical conductivity (σ) and Seebeck coefficients (S), which are necessary for good thermoelectric performance. Candidate materials are usually evaluated in terms of the dimensionless Figure of Merit ZT [2,3] given by $ZT=S^2\,\sigma/\kappa$. To maximise the energy generated by thermoelectrics, both, n and p −type elements are connected electrically in series and thermally in parallel within a thermoelectric module. The inherent toxicity, high cost and poor (high temperature) thermal stability of Te- and Pb-based alloys have limited the large-scale application of thermoelectric modules based on such materials. As alternatives to these well-known thermoelectric materials, oxides are attractive candidates because of their stability in air at high temperatures and low toxicity. However, their low electrical conductivity and high thermal conductivity limits their thermoelectric efficiency. Many attempts have been made to lower the thermal conductivity of well-known TE oxides through nanostructuring [4].

The naturally occurring superlattice structures found in the $ZnO\text{-}In_2O_3$ and $ZnO\text{-}Ga_2O_3$ systems has prompted interest in them as n −type oxide thermoelectrics [6-8]. The $Ga_2O_3(ZnO)_m$, $In_2O_3(ZnO)_m$ and $InGaO_3(ZnO)_m$ (m=integer) modular compounds are characterised by a stacked series of interfaces such as twin and inversion boundaries along their c −axis [7,9], which lowers the thermal conductivity, with respect to that of ZnO, by an order of magnitude [6, 7, 9]. The layered structures of these compounds enable good electrical conductivity in one direction, whilst maintaining effective scattering of phonons at the interfaces. This leads to enhanced ZT values when the anisotropy of these compounds is exploited by texturing [10]. A further advantage of these superlattice structures is the ease with which the width of the interfaces (structural modules) can be modified by changing the value of m, and thereby tuning their thermoelectric properties.

There have been limited studies on the thermoelectric properties and crystal structures of $Ga_2O_3(ZnO)_m$. In an early HRTEM study Li et al, [11] proposed a crystal structure for the end members with m=9 and 13 based on

gallium fully-occupied, wedge-shaped twin boundaries parallel to the *b* axis. They assigned the *Cmc2₁* space group on the basis of simulation and EDS techniques. In a single crystal XRD study of the $Ga_2O_3(ZnO)_m$ (*m=6* and 9) homologous compounds, Michiue et al [12] proposed the orthorhombic *Cmcm* group for even and odd values of *m* [6,13]. Subsequently, it was proposed by means of HRTEM that the $Ga_2O_3(ZnO)_9$ homologue [7,13] was formed by stacking of $m+1$ Zn-O tetrahedra, inversion boundaries (IB) and wedge-shaped twin boundaries (TB). The unique stacking sequence of IB and TB interfaces found in $Ga_2O_3(ZnO)_m$ efficiently scatter phonons, thereby reducing thermal conductivity. The effectiveness of these interfaces scattering phonons decreased the thermal conductivity to 1.8-1.3 W/m·K at 300-900 K when *m*=9, while maintaining an electrical conductivity of 10 S/cm and a Seebeck coefficient of -250 μV/K at room temperature [6,13].

The crystal structure of the $In_2O_3(ZnO)_m$ homologous compounds has been widely studied and consists of an alternate stacking of an InO_2^- octahedral layers with $(InZn_m)O_{m+1}^+$ layers [14-17]. The InO_2^- octahedral layer forms an inversion boundary (IB), where the polar c axis of the ZnO_4 octahedra within the $(InZn_m)O_{m+1}^+$ layers point backwards towards the InO_2^- octahedral layer. A zig-zag, In-rich modulated IB within the $(InZn_m)O_{m+1}^+$ layer has been proposed theoretically [16,17] and verified experimentally [14,15]. Electronic conduction within the $In_2O_3(ZnO)_m$ homologous compounds has been reported to occur mainly in the InO_2^- octahedral layers [18], leading to a high electrical conductivity of 500 S/cm at 300 K when *m*=5 [10]. Due to the highly anisotropic structure of these compounds, texturing is an effective way to enhance their thermoelectric response. A very high ZT of 0.33 was reported for a Yttria substituted $In_2O_3(ZnO)_5$ when textured [10].

In the Ga_2O_3-ZnO-In_2O_3 ternary system, the homologous compounds with the general formula $InGa_2O_3(ZnO)_m$ (m =2-20) exist [5, 14, 15, 19-21]. Using single crystal and powder X-ray diffraction analysis, a crystal structure closely similar to that of the $In_2O_3(ZnO)_m$ parental compound was proposed by Keller et al [21] for $InGaO_3(ZnO)_3$, with stacking of InO_2^- octahedral layers and $(GaZn_m)O_{m+1}^+$ layers; the Ga^{3+} atoms occupy the trigonal bipyramidal positions causing polarity inversion of the ZnO_4 tetrahedra at positions halfway between the InO_2^- octahedral layers. The proposed inversion boundary [21] formed by Ga^{3+} cations in trigonal bipyramidrons within the $(GaZn_m)O_{m+1}^+$ layer produces a flat boundary lying halfway between the InO_2^- octahedral layers.

The crystal structure in the $In_{1-x}Ga_xO_3(ZnO)_m$ (m=1-5) solid solution has also been reported. It was proposed [5] that the Ga atoms occupy the In sites in $(InZn_m)O_{m+1}^+$ for Ga substitutions equivalent to x=0.0-0.5, and start

substituting the In positions in the InO_2^- octahedral layer when $x>0.5$. Both the high electrical properties of the $In_2O_3(ZnO)_m$ compounds and the very low thermal conductivity of the $Ga_2O_3(ZnO)_m$ compounds encouraged us to investigate the thermoelectric properties of the $(Ga_{1-x}In_x)_2O_3(ZnO)_9$ solid solution. This solid solution should offer the advantage of reducing the processing cost over the $In_2O_3(ZnO)_9$ parent compound without compromising the thermoelectric response.

We have investigated the dependence of crystal structure and thermoelectric properties on composition in the $Ga_2O_3(ZnO)_9$ - $In_2O_3(ZnO)_9$ system. We identified that co-addition of B_2O_3 and Nd_2O_3 promotes densification in all the compositions. Clear correlations between the changes in the crystal structure and the transport properties have been established.

EXPERIMENTAL

Ceramics of $(1-x)Ga_2O_3(ZnO)_9$ - $xIn_2O_3(ZnO)_9$ (x=0.0 to 1.0 in steps of 0.2) were prepared. The starting powders were reagent grade ZnO (Prolabo, 99.9%) Ga_2O_3 (PI-KEM Ltd®, 99.995%) and In_2O_3 (PI-KEM Ltd®, 99.99%). The stoichiometric formulations were wet mixed with propan-2-ol, dried for 24 hours at 358 K, and then calcined in air at 1523 K for 4 h. After adding 0.2wt% B_2O_3 and 0.5wt% Nd_2O_3 to the calcined powders they were wet mixed again for 24 hours and dried. Calcined powders were uniaxially pressed into pellets 20 mm diameter and 4 mm thick using a hardened steel die. The pellets were covered in sacrificial powder of the same composition and then sintered at 1723 K for 4 h in air; the cooling and heating rates were 180 and 360 K/h, respectively. Densities of the sintered ceramics were determined by the Archimedes' method.

Phase identification and structural characterisation of the samples was performed using a PANalytical X'Pert Pro® diffractometer in Θ-Θ, Bragg-Brentano geometry with CuK_α radiation. Samples were scanned in the 2θ=25°-80° range with a step size of 0.017°. Spectra were refined using TOPAS-Academic V5® software [22].

For microstructure evaluation, specimens were ground and etched and examined using a Philips® XL30 (FEG)-SEM HKL® microscope equipped with an energy-dispersive X-ray (EDX) detector. Samples for TEM observations were crushed in an agate mortar and pestle. Grains of individual powders were dispersed in chloroform, dropped onto a copper grid covered with a holey carbon film, and then dried. Local structural characterisation of the samples was performed with a FEI FEG-TEM (Tecnai G2 F30) operating at 300 kV. Atomic-resolution Energy-dispersive X-ray spectroscopy (EDS) studies were carried out with a FEI Themis

Electron Microscope operated in STEM mode at 200 kV with a Super-X detector system (ChemiSTEM technology) for EDS chemical characterisation. EDS spectrum images were acquired by serially rastering across a defined area of the specimen, recording cumulative EDS spectra at each position. EDS chemical maps were produced by integrating the intensity of the Zn K_α and Ga K_α absorption peaks, respectively.

The electrical conductivity and Seebeck coefficients were determined as a function of temperature from ambient to 900 K in a helium atmosphere using an ULVAC® ZEM-III. Thermal diffusivity was determined from room temperature to 900 K in an argon environment using a Netzsch® LFA 427 laser flash analyser [23]; heat capacity was obtained using a Netzsch® STA 449 C. Finally, the thermal conductivity of the samples was calculated from the heat capacity (C_p), thermal diffusivity (α) and density (ρ), via the relationship $\kappa = \rho\alpha C_p$.

RESULTS AND DISCUSSION

With the exception of the $x = 0.6$ composition, all the $Ga_{1-x}In_xO_3(ZnO)_9$ ceramics attained a density of at least 90% theoretical. The one low density value of 85% theoretical (for x=0.6) relates to the mid-range of the $Ga_2O_3(ZnO)_9$ and $In_2O_3(ZnO)_9$ system. Nevertheless, 85% theoretical density for such compositions is still significantly higher than the values of 50-60% density reported by Moriga et al [5].

Fig. 1 shows microstructures of the $(Ga_{1-x}In_x)_2O_3(ZnO)_9$ polycrystalline ceramics sintered at 1723 K for 4 h. All the samples exhibit plate-like microstructures, typical of these layered compounds [7-10, 24]. Additionally, a minor second phase, white in colour was visible at the grain boundaries in all the samples (examples are red circled in Fig. 1a). Combined SEM-EDS analyses indicated the minor phases were rich in Nd. The segregation of this phase to the grain boundaries and the improved density (compared to earlier study of the ternary system [5]) suggests that successful liquid phase sintering was achieved through addition of 0.2wt% B_2O_3 and 0.5wt% Nd_2O_3. Stripes parallel to the growth direction are visible in some grains (Fig. 1c) in agreement with earlier investigations [8]; the number of grains exhibiting these parallel stripes decreases with increasing gallium concentration; the x=1 sample has a high density of these features (Fig. 1c). The size of grains in ceramics of the $(Ga_{1-x}In_x)_2O_3(ZnO)_9$ solid solution was independent of composition, being approximately 57 μm in all the samples.

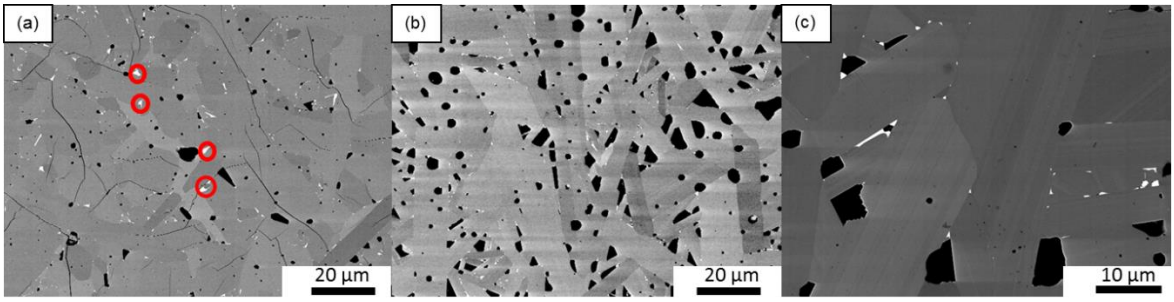

Fig. 1. *BSE/SEM images of* $(Ga_{1-x}In_x)_2O_3(ZnO)_9$ samples *(a) x=0.0, (b) x=0.1 and (c) high magnification image of sample x=1.0.*

Fig. 2 shows XRD spectra for the $(Ga_{1-x}In_x)_2O_3(ZnO)_9$ polycrystalline ceramics. Only peaks for the primary phase could be identified in the spectra. Diffraction data were indexed using a rhombohedral $R\bar{3}m$ space group proposed by Cannard and Tilley [25] and Keller et al. [21] for the $InGaO_3(ZnO)_9$ compounds and the *Cmcm* structure proposed for the $Ga_2O_3(ZnO)_9$ homologous compounds [9,12]. Even at low indium concentrations (x=0.2), the XRD spectra were indexed successfully using the rhombohedral $R\bar{3}m$ space group, typical of In-based homologous compounds; no traces of the orthorhombic *Cmcm* $Ga_2O_3(ZnO)_9$ variant were detected.

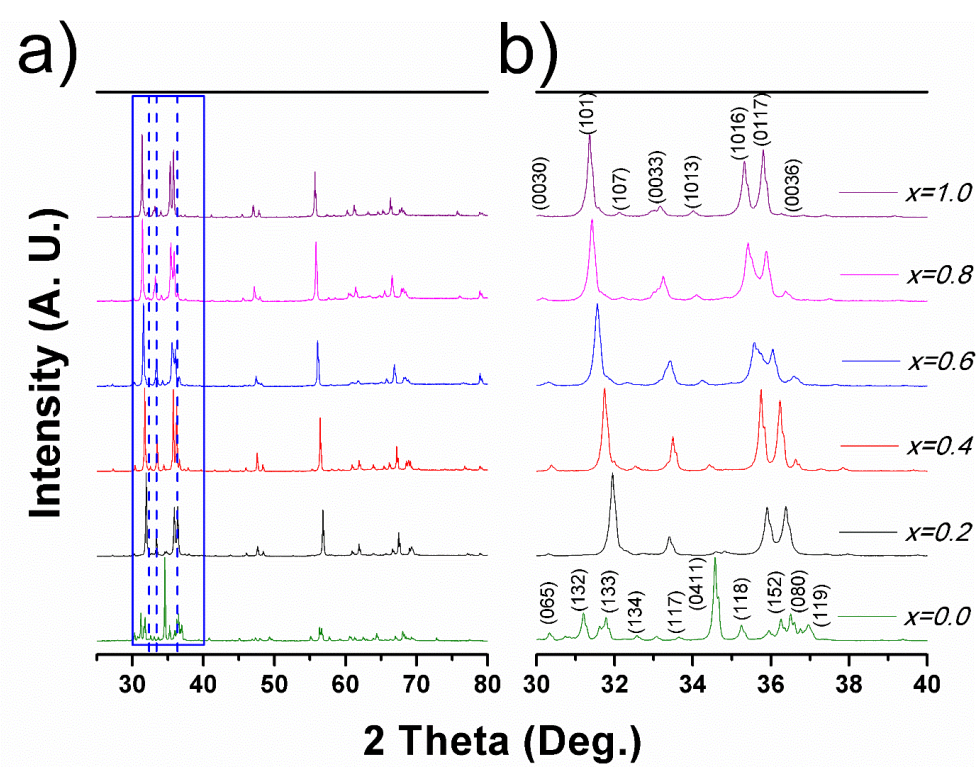

Fig. 2. XRD spectra of the $(Ga_{1-x}In_x)_2O_3(ZnO)_9$ samples for scan ranges of (a) 2θ=25-80°. and (b) 2θ=30-37°.

Increasing indium concentrations from x=0.2-0.4 caused a decrease in the lattice parameter c of the samples, whereas high indium concentrations (x=0.6-1.0) lead to an increase of the lattice parameter c. For low values of x these changes are reflected in the movements of the *(00l)* reflections towards higher 2θ values (Fig. 2b), consistent with the findings of Moriga et al. [5] for the $Ga_{1-x}In_x(ZnO)_m$ (m=3) system. Similarly, at higher indium content, increasing x from 0.6 to 1.0 displaces the $(00l)$ reflections towards lower 2θ values, indicating an increase in the lattice parameter c, in agreement with the work of Moriga et al. [5,20]. They suggested that at low indium concentrations (x<0.5), the reduction in the lattice parameter c is due to a compensation effect. When Ga atoms are substituted by In atoms in the InO_2^- layer of the $In_2O_3(ZnO)_m$ homologous compound, an expansion of the InO_2^- layer occurs in the a direction; this expansion is compensated by a contraction in the c direction to maintain the cation-anion distance [5,20]. In contrast, at high indium concentrations ($x > 0.5$), the lattice parameter c increases with indium concentration since larger indium atoms are substituting for smaller gallium atoms within the $(InZn_m)O_{m+1}^+$ layer [5,20]. The calculated lattice parameters are presented in Table I. The difference between the lattice parameter c for the x=0.2 and 1.0 samples is small (~1 Å). Nakamura and co-workers [19] predicted the length of the lattice parameter c (c_{Ref} in Table 1) to be 88.68 Å and 89.25 Å for x=0.2 and 1, respectively. They assumed a layered structure stacking InO_2^-, $(InZn)O_{2.5}$ and (m-1) ZnO layers along the c axis. These calculated values are slightly higher than our experimental values (c_{XRD}), summarised in Table 1, but the same trend is observed.

Table I. Lattice parameter c for $(Ga_{1-x}In_x)_2O_3(ZnO)_9$ samples from the XRD data (c_{XRD}), and calculated by Nakamura et al [19] (c_{Ref}).

SAMPLE	c_{XRD}(Å)	c_{Ref} (Å)[19]
$Ga_2O_3(ZnO)_9$	33.6355(6)	33.55
$(Ga_{0.8}In_{0.2})_2O_3(ZnO)_9$	88.4495(4)	88.68
$(Ga_{0.6}In_{0.4})_2O_3(ZnO)_9$	88.2186(2)	88.61
$(Ga_{0.4}In_{0.6})_2O_3(ZnO)_9$	88.4007(1)	88.39
$(Ga_{0.2}In_{0.8})_2O_3(ZnO)_9$	88.8735(5)	88.87
$In_2O_3(ZnO)_9$	89.006(2)	89.25

To better understand the structural changes induced by indium substitution, High Resolution Transmission Electron Microscopy (HRTEM) and Selected Area Electron Diffraction (SAED) analyses were performed. For the $Ga_2O_3(ZnO)_9$ end member, TEM images (e.g. Fig. 3a) revealed wedge shaped twin boundaries (TB), in agreement with the HRTEM studies of Li et al [11]. For the In-containing samples, the wedge shaped twin boundaries are no longer observed; instead equidistant parallel lines perpendicular to the c −axis (Fig. 3b,c) are observed even at low In concentrations (x=0.2). In the images m+1 atomic columns can be found in between the parallel lines, in agreement with earlier work on the ZnO-In_2O_3 based homologous compounds [19]. Similarly, HRTEM images for $In_2O_3(ZnO)_9$ end member (e.g. Fig. 3c) show equidistant parallel lines perpendicular to the c-axis (IB-I), corresponding to the InO_2^- octahedral layer inverting the polarity of the ZnO_4 tetrahedra along the basal plane [16,17,21,26]. A homogeneous distribution of m+1 atomic columns are observed in between these parallel lines within the $(InZn_m)O_{m+1}^+$ layer, highlighted by green spots in Fig. 3c. A less apparent zig-zag shaped structural feature, IB-II in Fig. 3c, can be observed within the $(InZn_m)O_{m+1}^+$ layer. This has been interpreted as In-rich pyramidal IB with a zig-zag shape and to be one dimensional modulated along the b axis [14,15]. The presence of the less apparent modulated zig-zagged IB is further confirmed by the appearance of additional satellite reflections around the main reflections in the SADP shown in Fig. 3c. The structure of the compound with the lowest Indium concentration (x=0.2) resembles the crystal structure exhibited by the $In_2O_3(ZnO)_m$ compounds (Fig. 3 c). It is believed that the formation of IBs in the basal plane, triggered by small additions of indium, are energetically more favourable than those in the pyramidal plane induced by gallium additions. The zig-zagged modulated pyramidal IB (IB-II) observed in the $In_2O_3(ZnO)_9$ compound is also preserved in $(Ga_{0.8}In_{0.2})_2O_3(ZnO)_9$. The presence of this IB type II is further confirmed by the appearance of additional spots in the SAED (Fig, 3b).

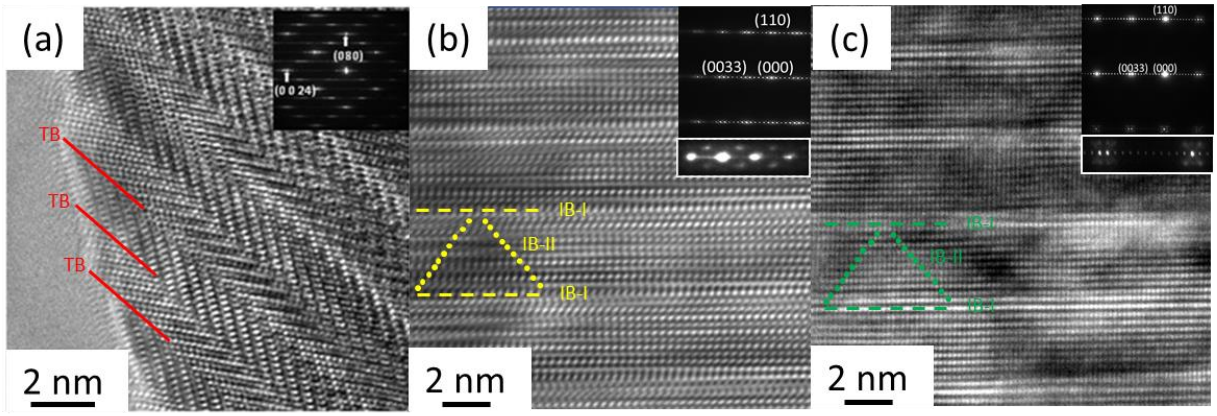

Fig. 3. (a) [100] HRTEM image of $Ga_2O_3(ZnO)_9$, (b) HRTEM [110] image of $(Ga_{0.8}In_{0.2})_2O_3(ZnO)_9$ and (c) HRTEM image of $In_2O_3(ZnO)_9$ homologous compound. The insets in the images show the corresponding SAED. Satellite reflections can be observed at the bottom of (b) in the enlarged SAED.

The crystal structure, the type of inversion boundaries, and the distribution of In in the lattice specifically in the inversion boundaries is well established [16,17,21,26]. To further distinguish the differences between the structural features exhibited by both end members, we conducted an aberration corrected microscopy study of the $Ga_2O_3(ZnO)_9$ sample (x=0), to resolve the structure and elemental distribution in the TB's and IB's. Fig. 4a shows a HAADF STEM image acquired with the incident electron beam parallel to the [100] direction; the image reveals a head to head type twinned nanostructure, with a wedge apex angle of ~63.37° (marked in Fig. 4a). The boundaries of the twins, labelled as TB in Fig. 3a, are parallel to the *b*- axis of the crystal structure. The deduced width of the twins from the lattice images is ~33 Å in agreement with HRTEM (see Fig. 3a). The well-ordered nano-TB are marked with parallel white lines (Fig. 4a). The $m + 1 = 10$ atomic columns in between the wedge shaped nano-TB boundaries are observed, as reported by Li et al in the earlier HRTEM studies [11]. The width of the nano-twins is uniform throughout the region screened in Fig. 3, corresponding to $m + 1 = 10$ atomic columns. The stacking sequence in the modular structure of the $Ga_2O_3(ZnO)_m$ compounds must be described by considering both the twin and inversion boundaries as structure building operators [7,9,12,13].

The distribution of Zn and Ga in the $Ga_2O_3(ZnO)_9$ structure was investigated by atomically resolved STEM-EDS; the maps (Fig. 4b,c) reveal the prevalence of Ga (and corresponding Zn depletion) at the TB, more specifically by the darker atomic columns in the HAADF image (Fig. 4a). The Ga partially-occupied TB observed in the HAADF-EDS maps (Figure 4 b,c) show that Ga and Zn occupy the alternate lattice sites in the twin boundaries. This finding is in good agreement with the predictions of Barf et al. [27], and HAADF-STEM-EDS study of Guilmeau et al. [7] on low level Ga doping of ZnO. Furthermore, Ga-enriched bands can be observed parallel and in between the TBs (Fig. 4b). These Ga-rich boundaries are inferred to be inversion boundaries. Thus, the EDS data suggests the formation of Ga-containing inversion boundaries in between the nano-TB boundaries.

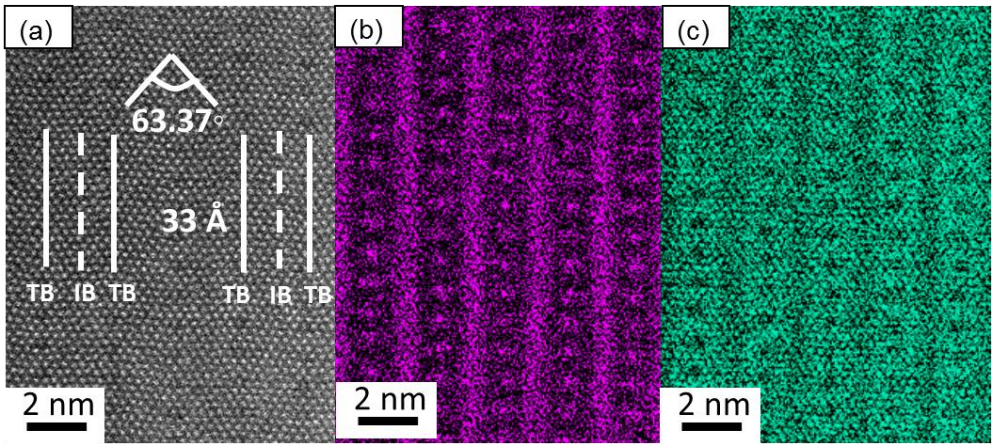

Fig. 4. (a) [100] HAADF image of the $Ga_2O_3(ZnO)_9$ (x=0) sample and corresponding EDS elemental maps for Ga-K_α (b) and Zn-K_α (c).

The thermoelectric properties of the (1-x)$Ga_2O_3(ZnO)_9$ - x$In_2O_3(ZnO)_9$ solid solution system were determined, and are summarised in Fig. 5. All the Ga-containing samples show semiconducting behaviour, with electrical conductivity 5-20 S/cm at room temperature. However, the $In_2O_3(ZnO)_9$ end member shows metallic behaviour with the highest electrical conductivity around 85 S/cm at room temperature; this is comparable with data reported by Ohta et al [8] for this end member. Overall, the electrical conductivity increases across the whole temperature range upon the introduction of In into the structure. Remarkably, the rate of increase of electrical conductivity with increasing temperature is more pronounced for composition x= 0.2, reaching a high value of 50 S/cm at 900 K. It is believed that the reasons for this beneficial increase in the electrical conductivity of $(Ga_{0.8}In_{0.2})_2O_3(ZnO)_9$ are (a) the change in the crystal structure from wedge shaped TB's to planar IB's and (b) a reduction in the electronic band gap [28]. The change in the crystal structure was triggered by the formation of both type I and type II inversion boundaries, creating a crystal structure similar to that of the $In_2O_3(ZnO)_9$ end member, as observed in Fig. 3b. At high gallium concentration (x<0.5) the IB-I, where the electrical conduction mainly occurs [18,20], will be highly doped by gallium. This substitution was previously proposed by Nakamura et al [19] and further confirmed by the systematic change in the lattice parameter c observed on our XRD data (Fig. 2). As well as the modification of the crystal structure (Fig. 3), the substitution of Ga at In sites may induce a change in the electronic band structure of $Ga_{1-x}In_xO_3(ZnO)_9$ due to the formation of localized band edge states by Ga additions [28]. The higher electrical conductivity at x=0.2 (Fig. 5a) further suggests the narrowing of the electronic band gap by the isoelectronic substitution of In for Ga at the inversion boundaries. Further increase in the indium concentration (x=0.4) also produces a high rate of increase of electrical

conductivity with increasing temperature, but less pronounced compared to samples with x=0.2 (Fig. 5). Additionally, the room temperature electrical conductivity of In-substituted compositions depends on the In-O bond lengths in the InO_2^- layer (IB-I); the larger the In-O distance, the higher the electrical conductivity as shown in Fig. 5a; this was proposed by Moriga et al [20] for the $InGaO_3(ZnO)_m$ m=1, 3 and 5 systems.

The Seebeck coefficients of the $(Ga_{1-x}In_x)_2O_3(ZnO)_9$ solid solution samples (Fig. 5b) exhibit $n-$type behaviour and the absolute values ($|S|$) increase with increasing temperature. Among all the compositions, the $In_2O_3(ZnO)_9$ end member shows the lowest $|S|$ which increased from 80 to150 μV/K over the temperature range, inversely proportional to the higher electrical conductivity exhibited by this sample. The Seebeck coefficients for the $In_2O_3(ZnO)_9$ sample are in good agreement with values reported by Ohta et al. [8] Within the uncertainty range, the Ga-based samples (x = 0.4, 0.6 and 0.8) have approximately the same Seebeck coefficients ($|S|$) which increase from ~150 μV/K at room temperature to ~250 μV/K at 900 K. The x=0.2 sample, $(Ga_{0.8}In_{0.2})_2O_3(ZnO)_9$, shows a slightly lower absolute value of the Seebeck coefficient, increasing from 110 to 180 μV/K over the temperature range tested. These results are consistent with the higher electrical conductivity exhibited by this sample (x=0.2).

The power factor for the $(Ga_{1-x}In_x)_2O_3(ZnO)_9$ solid solution samples are presented in Fig. 5c. Among the Ga based compounds, the $(Ga_{0.8}In_{0.2})_2O_3(ZnO)_9$ sample exhibited a much higher power factor of approximately 150 $\mu W/m\cdot K^2$ at 900 K compared to that of the $Ga_2O_3(ZnO)_9$ end member (75 $\mu W/m\cdot K^2$ at 900 K).

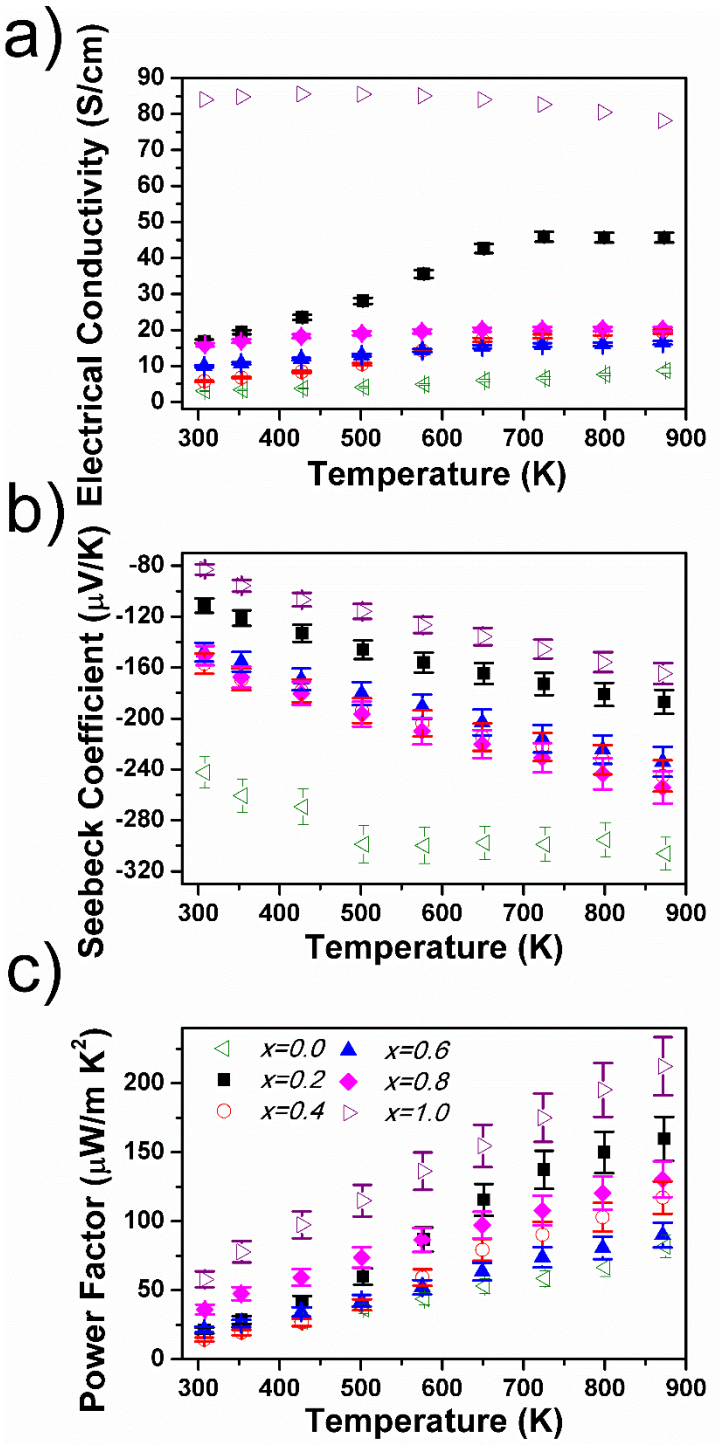

Fig. 5. (a) Electrical conductivity (b) Seebeck coefficient and (c) Power Factor of $(Ga_{1-x}In_x)_2O_3(ZnO)_9$ samples: ◁ x=0.0, ■ x=0.2, ○ x=0.4, ▲ x=0.6, ♦ x=0.8 and ▷ x=1.0.

The thermal conductivity of the $(Ga_{1-x}In_x)_2O_3(ZnO)_9$ samples are shown in Fig. 6a; all are less than 4 W/m·K at 300 K, which is much lower than for pure ZnO and most oxide-based thermoelectric materials. The thermal conductivity of the $Ga_{1-x}In_x)_2O_3(ZnO)_9$ samples gradually increased as the In concentration increased, reaching

3.7 W/m·K for x=1 at room temperature. The thermal conductivity of the x=0.6 sample is slightly lower than for the x=0.2 sample; this might be due to lower density of the x=0.6 sample (~85%). Moreover, considering Maxwell density corrections and the electronic contribution to the thermal conductivity, the lattice contribution to the thermal conductivity also increases as the In concentration increases in the $(Ga_{1-x}In_x)_2O_3(ZnO)_9$ system. This is attributed to the introduction of point defects at the interfaces (IB-I and IB-II). The thermal conductivity of the In-based compound is twice that of the Ga-based compound. However, low indium concentrations in the $(Ga_{1-x}In_x)_2O_3(ZnO)_9$ system significantly lowers the thermal conductivity of $In_2O_3(ZnO)_9$, approaching that of $Ga_2O_3(ZnO)_9$. This decrease in the thermal conductivity is ascribed to increased phonon scattering centres introduced through doping and the decreased distance in between the parallel interfaces IB-I (InO_2^- layer) when gallium substitutes for indium

The thermal conductivity of $In_2O_3(ZnO)_9$ (x=1.0), Fig. 6a, is 12% lower than the value reported by Ohta et al. [8]. The calcination step and longer sintering time used in this study may be the reason for this beneficial reduction. However, the mechanism lowering the thermal conductivity of our high-density sample can not be identified by simple comparison with the work of Ohta et al [8], due to the lack of structural and microstructure details in their study.

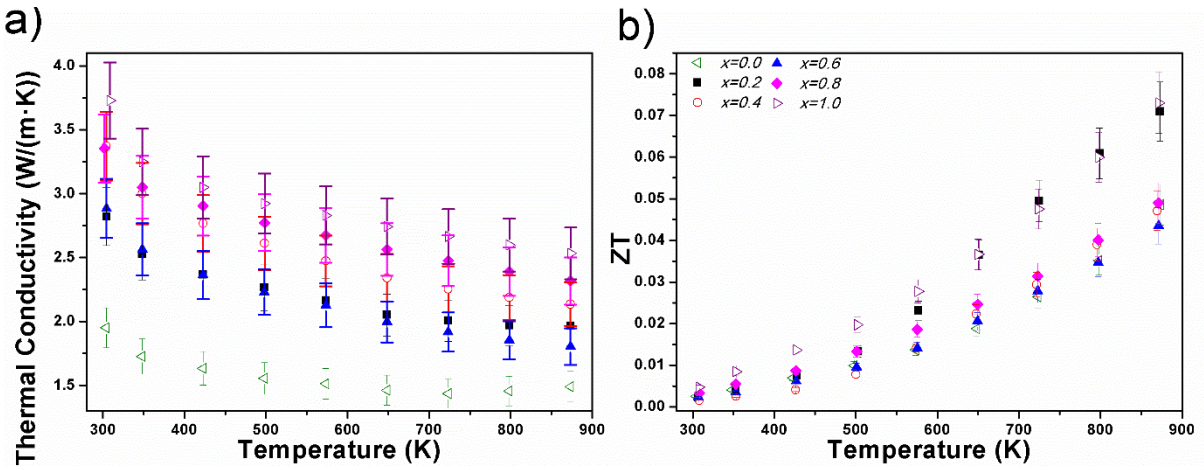

Fig. 6. (a) Thermal conductivity and (b) Dimensionless figure of merit of $(GaIn_{1-x}In_x)_2O_3(ZnO)_9$ *samples*: ◁ x=0.0, ■ x=0.2, ○ x=0.4, ▲ x=0.6, ♦ x=0.8 and ▷ x=1.0.

The Figure of Merit for all the samples was determined from the power factor and thermal conductivity data (Fig. 5 and 6a) and is plotted in Fig. 6 b. In the In-substituted samples, a high Figure of Merit of 0.07 at 900 K was obtained for $(Ga_{0.8}In_{0.2})_2O_3(ZnO)_9$ sample. This is due to improved power factor while maintaining the low

thermal conductivity of $(Ga_2O_3(ZnO)_9$ achieved by engineering the interfaces at the nanoscale level. The reduced thermal conductivity of composition x=0.2 is ascribed to increased phonon scattering centres introduced through mass difference and the reduction in the spacing of the interfaces. The high figure of merit for the x= 0.2 sample (Fig. 6b) of 0.07 is the highest reported for the In and Ga homologous compounds; $(Ga_{1-x}In_x)_2O_3(ZnO)_m$ (x=0.5, m= 1, 3 and 5) [9,20] and $In_2O_3(ZnO)_9$. This high ZT of 0.07 at 900 K arises from the lower thermal conductivity exhibited by the high density $In_2O_3(ZnO)_9$ compound prepared with 0.2wt% B_2O_3 and 0.5wt% Nd_2O_3.

CONCLUSIONS

High density ceramics in the $(Ga_{1-x}In_x)_2O_3(ZnO)_9$ system were achieved by the use of minor additions of B_2O_3 and Nd_2O_3 to promote densification. The structural features of Ga-based compounds are different from the In-based compounds. The $Ga_2O_3(ZnO)_9$ stacks twin and inversion boundaries along the c axis whereas the $In_2O_3(ZnO)_9$ is formed by the stacking of basal and pyramidal inversion boundaries [26]. It was found, that even at low Indium concentrations (x=0.2), the crystal structure of the $(Ga_{1-x}In_x)_2O_3(ZnO)_9$ homologue resembles that of the $In_2O_3(ZnO)_m$ end member rather than its gallium counterpart. The sample with the lowest indium concentration (x=0.2) exhibited basal and pyramidal zig-zag shaped IB's, typically found in the $In_2O_3(ZnO)_m$ family. The presence of gallium and indium at these inversion boundaries increased the number of scattering centres, lowering the thermal conductivity. Substitution of small amounts of In (i.e $(Ga_{0.8}In_{0.2})_2O_3(ZnO)_9$ x=0.2), significantly improved the thermoelectric properties of $Ga_2O_3(ZnO)_9$ end member; the Seebeck coefficients increased from (160 to 185 μV/K at 900K), electrical conductivity increased from (~5 to 40 S/cm at 900 K) while maintaining a low thermal conductivity of 2 W/m·K at 900 K leading to a high figure of merit of 0.07 at 900 K; this is the highest ZT reported for both Ga- and In-based homologous compounds. The ZT of the x=0.2 sample is as high as that for samples of $In_2O_3(ZnO)_9$, with the added benefit of reduced processing costs through engineering the interfaces at the nanoscale level.

ACKNOWLEDGMENTS

The authors are grateful to the EPSRC for the provision of funding for this work (EP/H043462, EP/I036230/1, EP/L014068/1, EP/L017695/1 acknowledged by RF). SuperSTEM is the EPSRC National Facility for

Advanced Electron Microscopy, supported by EPSRC. PS and PS Sr. acknowledge the support of the projects APVV-15-0049 and VEGA 2/0082/17

REFERENCES

1. H. J. Goldsmid, and R. W. Douglas, Brit. J. Appl. Phys. 11, 386 (1954).
2. V. E. Altenkirch, Physik. Zeitschr. 16, 560 (1909).
3. V. E. Altenkirch, Physik. Zeitschr. 12, 920 (1911).
4. S. R. Yeandel, M. Molinari, and S. C. Parker, RSC Adv. 6, 114069 (2016).
5. T. Moriga, D. R. Kammler, T. O. Mason, G. B. Palmer, and K. R. Poeppelmeier, J. Am. Ceram. Soc. 82, 2705 (1999).
6. Y. Michiue, T. Mori, A. Prytuliak, Y. Matsushita, M. Tanaka, and N. Kimizukac, RSC Adv. 1, 1788 (2011).
7. E. Guilmeau, P. Díaz-Chao, O. I. Lebedev, A. Rečnik, M. C. Schäfer, F. Delorme, F. Giovannelli, M. Košir, and S. Bernik, Inorg. Chem. 56, 480 (2017).
8. H. Ohta, W. S. Seo, and K. Koumoto, J Am Ceram Soc. 79, 2193 (1996).
9. D. T. Alvarez -Ruiz, F. Azough, D. Hernandez-Maldonado, D. M. Kepaptsoglou, Q. M. Ramasse, S. J. Day, P. Svec, P. Svec Sr., and R. Freer, J Alloys Compd. 762. 892 (2018).
10. S. Isobe, T. Tani, Y. Masuda, W. S. Seo,and K. Koumoto, Jpn J Appl Phys. Part 1, 41,731 (2002).
11. C. Li, Y. Bando, M. Nakamura, M. Onoda, and N. Kimizuka, J. Solid State Chem. 139, 213 (1998).
12. Y. Michiue, and N. Kimizuka, Acta Crystallogr Sec B.66, 117 (2010).
13. D. T. Alvarez-Ruiz, Doctoral thesis, University of Manchester (2018).
14. C. Li, Y. Bando, M. Nakamura, and N. Kimizuka, J Electron Microscopy. 46, 119 (1997).
15. C. Li, Y. Bando, M. Nakamura, M. Onoda, and N. Kimizuka, J Solid State Chem.139, 213 (1998).
16. Y. Yan, L. F. Juarez-Da Silva, S. H. Wei, and M. Al-Jassim, Appl. Phys. Lett. 90, 261904 (2007).
17. Y. Yan, A. Walsh, L. F. Juarez-Da Silva, S. H. Wei, and M. Al-Jassim, in 34th IEEE Photovoltaic Specialists Conference (2009), pp. 000172-000174.
18. A. Yoshinari, K. Ishida, K. I. Murai, and T. Moriga, Mat. Res. Bull. 44, 432 (2009).
19. M. Nakamura, N. Kimizuka, and T. Mori, J Solid State Chem. 93, 298 (1991).

20. T. Moriga, K. Ishida, K. Yamamoto, A. Yoshinari, and K. I. Murai, Mater. Res. Innovations. 13, 348 (2009).
21. I. Keller, W. Assenmacher, G. Schnakenburg, and W. Mader, Z. Anorg. Allg. Chem. 635, 2065 (2009).
22. A. Coelho, Topas Academic V5, Brisbane, Australia, (2014).
23. R. Taylor, J Phys E. 13, 1193 (1980).
24. S. W. Yoon, J. H. Seo, T. Y. Seong, T. H. Yu, Y. H. You, K. B. Lee, H. Kwon, and J. P. Ahn, Cryst Growth and Design. 12, 1167 (2012).
25. P. J. Cannard, and R. J. D. Tilley, J Solid State Chem.73, 418 (1988).
26. J. B. Labegorre, O. I. Lebedev, C. Bourge, A. Recnik, M. Kosir, S. Bernik, A. Maignan, T. Le Mercier, L. Pautrot-d'Alencon, and E. Guilmeau, ACS Appl. Mater. Interfaces. 10, 6415 (2018).
27. J. Barf, T. Walther, and W. Mader, Int Sci. 12, 213 (2004).
28. Y. Liu, W. Xu, D-B Liu, M. Yu, Y-H Lin, and C-W Nan, Phys. Chem. Chem. Phys., 17, 11229 (2015).